

Nonreciprocal Phonon Propagation in a Metallic Chiral Magnet

T. Nomura,^{1,*} X.-X. Zhang,² R. Takagi,^{3,4} K. Karube,² A. Kikkawa,²
Y. Taguchi,² Y. Tokura,^{2,3,5} S. Zherlitsyn,⁶ Y. Kohama,¹ and S. Seki^{3,4}

¹*Institute for Solid State Physics, University of Tokyo, Kashiwa, Chiba 277-8581, Japan*

²*RIKEN Center for Emergent Matter Science (CEMS), Wako 351-0198, Japan*

³*Department of Applied Physics, The University of Tokyo, Tokyo 113-8656, Japan*

⁴*PRESTO, Japan Science and Technology Agency (JST), Kawaguchi 332-0012, Japan*

⁵*Tokyo College, University of Tokyo, Tokyo 113-8656, Japan*

⁶*Hochfeld-Magnetlabor Dresden (HLD-EMFL), Helmholtz-Zentrum Dresden-Rossendorf, 01328 Dresden, Germany*

(Dated: December 2, 2022)

The phonon magnetochiral effect (MChE) is the nonreciprocal acoustic and thermal transports of phonons caused by the simultaneous breaking of the mirror and time-reversal symmetries. So far, the phonon MChE has been observed only in a ferrimagnetic insulator Cu_2OSeO_3 , where the nonreciprocal response disappears above the Curie temperature of 58 K. Here, we study the nonreciprocal acoustic properties of a room-temperature ferromagnet $\text{Co}_9\text{Zn}_9\text{Mn}_2$ for unveiling the phonon MChE close to the room temperature. Surprisingly, the nonreciprocity in this metallic compound is enhanced at higher temperatures and observed up to 250 K. This clear contrast between insulating Cu_2OSeO_3 and metallic $\text{Co}_9\text{Zn}_9\text{Mn}_2$ suggests that metallic magnets have a mechanism to enhance the nonreciprocity at higher temperatures. From the ultrasound and microwave-spectroscopy experiments, we conclude that the magnitude of the phonon MChE of $\text{Co}_9\text{Zn}_9\text{Mn}_2$ mostly depends on the magnon bandwidth, which increases at low temperatures and hinders the magnon-phonon hybridization. Our results suggest that the phonon nonreciprocity could be further enhanced by engineering the magnon band of materials.

When a chiral material is placed in a magnetic field, nonreciprocal properties arise from the simultaneous breaking of the mirror and time-reversal symmetries. Such nonreciprocal properties are due to magnetochiral effect (MChE) [1, 2] observed for various (quasi)particle propagations, including photons [3–8], electrons [9–14], magnons [15–19], and phonons [20]. For the case of phonons, the sound velocity in a chiral material becomes different for parallel and antiparallel propagations with respect to the magnetic field \mathbf{H} [20]. Because of the symmetry origin, the MChE is expected for any chiral materials although the microscopic mechanism and magnitude depend on the system. Since the nonreciprocal properties are closely related to functionalities, the MChE is an attractive mechanism for novel devices (ex. single-phase diodes and circulators).

So far, the phonon MChE has been reported only for the ferrimagnetic insulator Cu_2OSeO_3 [20]. The phonon MChE is explained by a magnon-phonon hybridization [20, 21]. Because of the Dzyaloshinskii-Moriya (DM) interaction, the magnon dispersion in Cu_2OSeO_3 is asymmetric for wave vector \mathbf{k} parallel and antiparallel to \mathbf{H} [15, 22]. When the magnon-phonon hybridization is allowed by symmetry, the phonon dispersion is asymmetrically deformed by the band repulsion, leading to the nonreciprocal sound velocity for $\pm\mathbf{k}$ [Fig. 1(a)]. In this case, the MChE is observed only below the Curie temperature $T_C \sim 58$ K [23, 24]. For realizing the MChE at room temperature, experimental exploration on higher- T_C magnets is important. Moreover, the investigation of

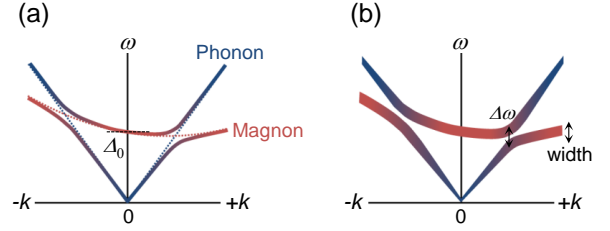


FIG. 1. Phonon MChE caused by the magnon-phonon hybridization. (a) Dispersion relations of the magnon and acoustic-phonon bands near the Γ point. (b) Effect of the magnon-dispersion broadening. Note that only one of the circularly polarized phonon mode hybridizes with magnons, since only right-handed polarization exists for ferromagnetic-type spin waves with respect to the magnetization. The ultrasound frequency in this study was always much smaller than the magnon gap $\Delta_0/2\pi$.

metallic magnets allows for exploring the phonon nonreciprocity in presence of conduction electrons.

Our target material $\text{Co}_9\text{Zn}_9\text{Mn}_2$ has a β -Mn-type structure, which belongs to the chiral space group $P4_132$ ($P4_332$) [25, 26]. The magnetic properties of the series of $(\text{Co}_{0.5}\text{Zn}_{0.5})_{20-x}\text{Mn}_x$ alloys have been systematically studied, and various exciting properties related to their chiral magnetism have been reported [16, 27–38]. Among this series, $\text{Co}_9\text{Zn}_9\text{Mn}_2$ has a high Curie temperature $T_C \sim 400$ K. $\text{Co}_9\text{Zn}_9\text{Mn}_2$ has a helimagnetic ground state, while other Mn-rich compounds become spin glass at low temperature due to the geometrical frustration [32]. The spin-glass state could complicate the analysis of the magnon dispersion and its temperature depen-

* t.nomura@issp.u-tokyo.ac.jp

dence. In addition, the magnon MChE and the magnon dispersion of $\text{Co}_9\text{Zn}_9\text{Mn}_2$ have already been studied [16]. Therefore, $\text{Co}_9\text{Zn}_9\text{Mn}_2$ is a promising system to explore the room-temperature phonon MChE.

Single crystals of $\text{Co}_9\text{Zn}_9\text{Mn}_2$ were grown by the Bridgman method as described in our previous papers [28, 29, 32]. For the ultrasound measurements, we used a right-handed single crystal ($P4_132$) with the sample length of 1.9 mm along the $[110]$ axis. We employed the ultrasound pulse-echo technique with a phase-sensitive detection for the sound-velocity measurement [39]. In this study, we investigated three acoustic modes $c_L = (c_{11} + c_{12} + 2c_{44})/2$ ($\mathbf{k} \parallel \mathbf{u} \parallel [110]$, $v = 4.0$ km/s), $c_T = (c_{11} - c_{12})/2$ ($\mathbf{k} \parallel [110]$, $\mathbf{u} \parallel [1\bar{1}0]$, $v = 2.1$ km/s), and c_{44} ($\mathbf{k} \parallel [110]$, $\mathbf{u} \parallel [001]$, $v = 2.4$ km/s), where \mathbf{k} and \mathbf{u} are the propagation and displacement vectors, respectively. We used the ultrasound frequency up to 530 MHz by high-harmonic generation of the LiNbO_3 resonance transducers. In this study, the experiments were performed in the Faraday geometry with $\mathbf{H} \parallel \mathbf{k} \parallel [110]$. In addition, we performed the microwave absorption spectroscopy on a crystal from the same batch. The microwave absorption (ΔS_{11}) caused by magnetic resonance was monitored by using a coplanar waveguide and a vector-network analyzer. For details, see Refs. [16, 40].

Figure 2(a) shows the magnetic-field dependence of the relative change of the sound velocity $\Delta v/v_0$ of the c_{44} acoustic mode at 4 and 250 K. The magnetic transition from a helical to a collinear state is observed at $H_c = 0.21$ T (4 K) and 0.14 T (250 K). The sound velocities for $-\mathbf{k}$ and $+\mathbf{k}$ at H_c are slightly different, indicating the nonreciprocal sound propagation. The sign of the difference becomes opposite for $-H_c$ and $+H_c$, which is the characteristic feature of the phonon MChE. We note that the other acoustic modes (c_L and c_T) show weaker $\Delta v/v_0$ and nonreciprocal responses, indicating the weaker magnetoelastic coupling. These results are presented in the Supplemental Material (SM) [41].

Figure 2(b) plots the results for $-\mathbf{k}$ as a function of the absolute value of the magnetic field. The magnitude of the phonon magnetochiral effect g_{MCh} defined as [20]

$$g_{\text{MCh}}(H) = \frac{\Delta v(+\mathbf{H})}{v_0} - \frac{\Delta v(-\mathbf{H})}{v_0} = \frac{v(+\mathbf{H}) - v(-\mathbf{H})}{v_0} \quad (1)$$

is plotted in the lower panel. The nonreciprocal response takes maximum at H_c , and then rapidly decreases when the field is further increased. The nonreciprocal magnitude at the transition field $g_{\text{MCh}}(H_c)$ as a function of the ultrasound frequency is plotted in Fig. 2(c). The nonreciprocity nonlinearly enhances at higher frequencies. $g_{\text{MCh}}(H_c)$ at 250 K is larger than that at 4 K. The contour plot of g_{MCh} at 440 MHz is mapped on the T - H phase diagram [Fig. 3(a)].

The experimental results show that the magnetochiral effect of $\text{Co}_9\text{Zn}_9\text{Mn}_2$ is enhanced at H_c and at higher ultrasound frequency. Similar features are observed in Cu_2OSeO_3 and explained by the magnon-phonon hybridization mechanism [20]. The magnon dispersion of

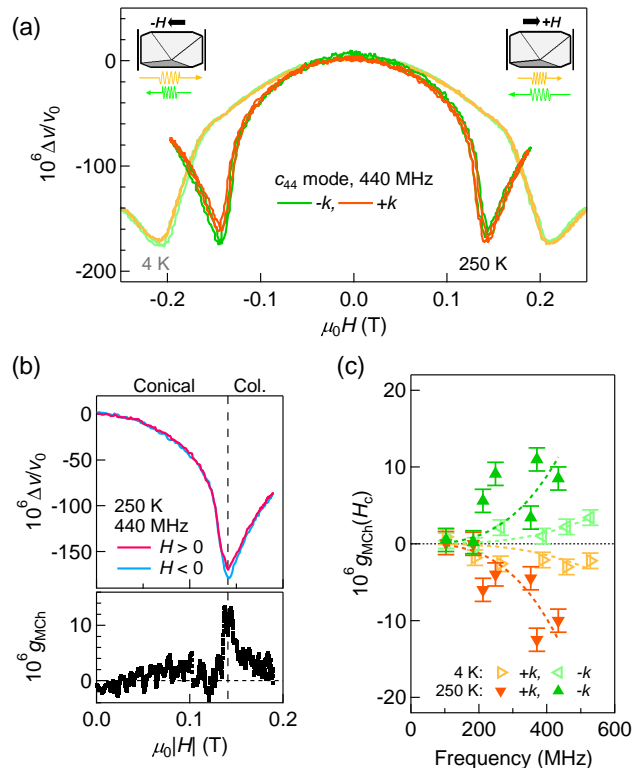


FIG. 2. Phonon MChE in $\text{Co}_9\text{Zn}_9\text{Mn}_2$. (a) Relative change of the sound velocity as a function of magnetic field, $\Delta v/v_0(H)$, of the c_{44} acoustic mode at the ultrasound frequency of 440 MHz. Schematics of the experimental configuration and the nonreciprocity are shown. (b) $\Delta v/v_0(H)$ and the magnitude of the magnetochiral effect g_{MCh} as a function of the absolute value of the magnetic field. The data for $-\mathbf{k}$, 440 MHz at 250 K from Fig. 2(a) are used. (c) Ultrasound frequency dependence of the magnitude of the magnetochiral effect at the transition field $g_{\text{MCh}}(H_c)$. The results for the c_{44} mode at 4 and 250 K are fitted by Eq. (2) (dashed lines).

$\text{Co}_9\text{Zn}_9\text{Mn}_2$ is also asymmetric for $\pm\mathbf{k}$ because of the DM interaction [16]. When such magnon band hybridizes with a phonon band, the anticrossing asymmetrically deforms the phonon band [Fig. 1(a)], leading to the nonreciprocal acoustic properties. At the conical-collinear transition, the magnon gap becomes small, and the hybridization occurs close to the Γ point (Fig. 1). However, the magnon frequency is more than one order of magnitude higher than the ultrasound frequency in this study, and only the effect due to the band repulsion is observed in our experiments. Here, we emphasize that the electron-phonon hybridization cannot explain the characteristic enhancement of the phonon MChE at H_c , because the electronic band structure does not change as a function of magnetic field in the collinear phase.

The magnon-phonon hybridization is mediated by shear strains which modulate the DM interactions. The

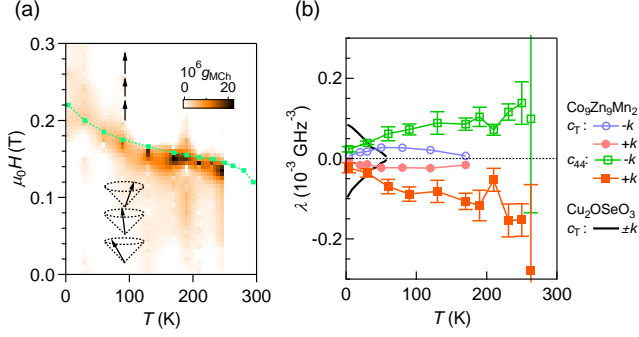


FIG. 3. (a) Contour plot of g_{MCh} mapped on the T - H phase diagram. The conical-collinear phase boundary (green curve) is determined by the anomalies in $\Delta v/v_0$. Here, the results at 440 MHz are used. (b) Temperature dependence of the magnitude of the phonon MChE. The coefficient λ is obtained by fitting the frequency dependence of $g_{\text{MCh}}(H_c)$ [Fig. 2(c)]. The results of Cu_2OSeO_3 [20] are shown for comparison.

magnitude of the MChE is expressed as [20],

$$g_{\text{MCh}} = \frac{4\gamma^2 \langle S^z \rangle^2 S^2 D^3 k^3}{c\Delta_0^2} = \lambda f^3. \quad (2)$$

Here, γ , S , D , c , Δ_0 are the magnetoelastic coupling constant, the total spin moment, the DM-interaction coefficient, the elastic constant, and the magnon gap, respectively. Since the wave vector k is proportional to the ultrasound frequency f , the equation is rewritten as the empirical form with the phonon-MChE coefficient λ .

Based on Eq. (2), the frequency dependence of $g_{\text{MCh}}(H_c)$ [Fig. 2(c)] is fitted and the temperature dependence of λ is obtained as Fig. 3(b). The MChE is observed up to 170 K and 250 K for the c_T and c_{44} modes, respectively. $|\lambda|$ is always larger for the c_{44} than that for the c_T mode, which again indicates the stronger magnetoelastic coupling of the c_{44} mode. $|\lambda|$ of the c_{44} mode increases towards higher temperatures and suddenly becomes undetectable at 260 K. This is because of the sudden decrease of $\Delta v/v_0(H_c)$ and increase of the acoustic attenuation around this temperature [41]. This characteristic temperature might be due to the decreased anisotropy at high temperatures or either due to the extrinsic origins, *i.e.* glass transition of the glue connecting the transducers and the sample. In the last case, the phonon MChE might be detected above 260 K by the thermal transport [42]. For a quantitative comparison, the results of Cu_2OSeO_3 [$c_T = (c_{11} - c_{12})/2$ mode] [20] are plotted by the black lines. The maximum value of λ in $\text{Co}_9\text{Zn}_9\text{Mn}_2$ is larger than that in Cu_2OSeO_3 by the factor of ~ 1.5 . $|\lambda|$ is tending to increase with temperature in $\text{Co}_9\text{Zn}_9\text{Mn}_2$, though it is decreasing in Cu_2OSeO_3 [Fig. 3(b)]. In the following, we discuss the reason of the different temperature dependence by comparing the case of insulator (Cu_2OSeO_3) and metal ($\text{Co}_9\text{Zn}_9\text{Mn}_2$).

The negative- T coefficient of $|\lambda|$ for Cu_2OSeO_3 is due to the temperature dependence of the ordered moment

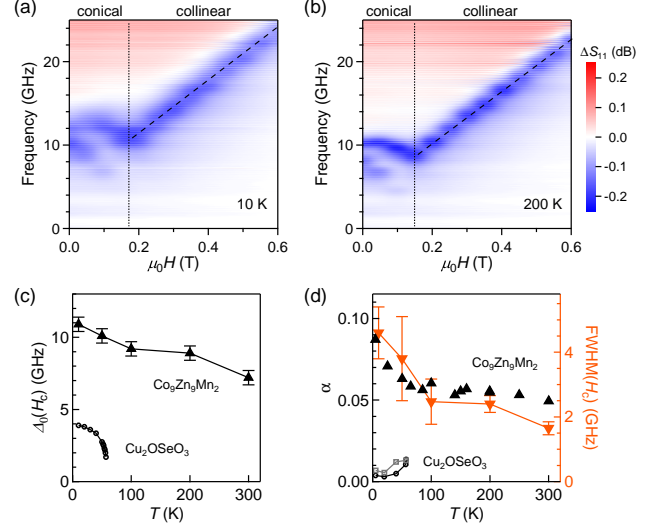


FIG. 4. Magnetic-field dependence of the microwave-absorption spectra (ΔS_{11}) at (a) 10 K and (b) 200 K. The ferromagnetic resonance lines are shown by the dashed lines for guide. The conical-collinear phase boundary is shown by the dotted line. (c) Temperature dependence of the magnon-gap frequency at the transition field. (d) Temperature dependence of the Gilbert damping coefficient α (left) and the FWHM at the transition field (right). The results for Cu_2OSeO_3 are taken from Ref. [43] and shown for comparison. Square (circle) symbols represent the result for $\mathbf{H}||[111]$ ($\mathbf{H}||[100]$). α of $\text{Co}_9\text{Zn}_9\text{Mn}_2$ is taken from Ref. [36].

$\langle S^z \rangle$ [20]. Near the magnetic phase transition, $\langle S^z \rangle$ scales as $\sqrt{|T - T_C|}$, leading to the T -linear dependence of g_{MCh} [Eq. (2)]. For the case of $\text{Co}_9\text{Zn}_9\text{Mn}_2$, the temperature dependence of $\langle S^z \rangle$ is negligible below 200 K because of the high Curie temperature $T_C \sim 400$ K [32]. Therefore, the positive- T coefficient of $|\lambda|$ originates from other properties.

Another T -dependent parameter in Eq. (2) is the magnon gap Δ_0 . Figures 4(a) and 4(b) show the microwave-absorption spectra as a function of magnetic field at 10 K and 200 K, respectively. With this technique, the obtained spectra reflect the magnon gap at $k = 0$. The overall features at 10 K and 200 K are similar. In the helical phase, two branches of spin waves soften towards H_C . In the collinear phase, single absorption peak linearly increases as a function of magnetic field (dashed line). Slight temperature dependence is observed in the magnon gap and width of the absorption peak. Figure 4(c) plots the temperature dependence of the magnon gap at the transition field $\Delta_0(H_c)$. For comparison, the results of Cu_2OSeO_3 are also shown [43]. The gap of $\text{Co}_9\text{Zn}_9\text{Mn}_2$ increases towards lower temperatures by the factor of ~ 1.2 , which would lead to the decrease of $g_{\text{MCh}}(H_c)$ by the factor of 1.4 [Eq. (2)]. This parameter cannot account for the observed factor of $\lambda(200 \text{ K})/\lambda(10 \text{ K}) \sim 10$ [Fig. 3(b)].

Next, the temperature dependence of the full width at

TABLE I. Summary of the magnetic and elastic parameters. The unit cells of $\text{Co}_9\text{Zn}_9\text{Mn}_2$ and Cu_2OSeO_3 are taken per Co ion and per 4Cu cluster, respectively. The last column presents the calculated coefficient of the phonon MChE based on Eq. (2).

	S	a_0 (Å)	D/a_0^2 (J m^{-2})	$\Delta_0(H_c)/2\pi$ (GHz)	FWHM(H_c) (GHz)	c (GPa)	$g_{\text{MCh}}/\gamma^2 k^3$ (m^3)
$\text{Co}_9\text{Zn}_9\text{Mn}_2$ (200 K) [16, 29]	0.75	3.1	1.2×10^{-3}	8.9	2.4	$c_{44} = 45$	43×10^{-30}
$\text{Co}_9\text{Zn}_9\text{Mn}_2$ (10 K)				10.9	4.6	$c_{44} = 47$	
Cu_2OSeO_3 (30 K) [15]	0.44	4.5	3.4×10^{-4}	3.7	0.4	$c_T = 27$	11×10^{-30}

half maximum (FWHM) of the magnetic resonance at H_c is plotted in Fig. 4(d) right axis with orange triangles. The broadening of the absorption peak is observed below 100 K. The width of the magnon absorption (Δf) is related to the Gilbert damping parameter α as [43, 44]

$$\Delta f = 2\alpha f_r + \Delta f_0, \quad (3)$$

where f_r is the resonance frequency and Δf_0 is the extrinsic broadening. The Gilbert damping parameters of $\text{Co}_9\text{Zn}_9\text{Mn}_2$ [36] and Cu_2OSeO_3 [43] are plotted in Fig. 4(d) left axis. The temperature dependence of α and the width of the magnon absorption is well scaled. The magnon damping of $\text{Co}_9\text{Zn}_9\text{Mn}_2$ enhances towards lower temperatures. This is a typical behavior for magnetic alloys, where magnons are scattered by conduction electrons [44, 45]. At lower temperature, the electron scattering time increases and the larger momentum transfer at the intraband relaxation results in the enhanced damping. For the case of $\text{Co}_9\text{Zn}_9\text{Mn}_2$, disorder of Mn spins at low temperatures might also be the reason of the increased α [36]. On the other hand, for the case of magnetic insulators, the magnon-phonon and magnon-magnon scatterings are suppressed at lower temperatures, leading to the smaller α . Therefore, the opposite temperature dependence of α is a clear contrast between magnetic insulators and metals, which is a key to understand the temperature dependence of the phonon MChE of $\text{Co}_9\text{Zn}_9\text{Mn}_2$.

A hybridized state of a magnon and a phonon is called a magnon polaron [46–48]. When the magnon scattering time τ is too short to well form the hybridized state (namely α is too large), the anticrossing gap $\Delta\omega$ is effectively reduced. For instance, when $1/\tau \gg \Delta\omega$, the magnon-polaron bands become more smeared and short-lived in this weak-coupling case [46]. Substituting $\tau = 1/\alpha\omega$, this condition reads $\alpha \gg \Delta\omega/\omega$. The anticrossing gap is estimated as (see SM for details [41]),

$$\Delta\omega = \frac{\gamma \langle S^z \rangle \sqrt{SD}}{a_0^2 \sqrt{\rho s v_0^2}} \omega^{* \frac{3}{2}}, \quad (4)$$

where a_0 , ρ , $s = \hbar/V_0$, and ω^* are the lattice constant, the mass density, the reduced Planck constant normalized by the unit-cell volume, and the angular frequency at the hybridization point. Substituting the parameters of $\text{Co}_9\text{Zn}_9\text{Mn}_2$, $\Delta\omega/2\pi$ is estimated to be of the order of 10 MHz, using $\gamma \sim 10$. The estimated $\Delta\omega/\omega$ is of the

order of 10^{-3} , which is consistent with $\Delta v/v_0 \sim 10^{-4}$ because one can roughly use $\omega = vk$ for small k . Therefore, the damping factor $\alpha \sim 0.1$ is much larger than $\Delta\omega/\omega$, indicating that the magnon-phonon hybridization occurs in a weak coupling regime. In this case, the magnon linewidth (and the magnon scattering time) can considerably affect the hybridization. Indeed, the anomaly at the phase transition $\Delta v(H_c)/v_0$ decreases below 100 K where α also increases (Fig. S1(b) [41]), indicating the weaker magnon-phonon hybridization. Such an effectively weaker magnon-phonon coupling accordingly leads to smaller anticrossing gap and also reduces nonreciprocity g_{MCh} . Quantitative relation of how α affects g_{MCh} exceeds the present theory based on sharp magnon-polaron bands and is left for future investigation.

The above discussion suggests that the phonon MChE can be further enhanced by reducing the magnon linewidth, which is related to the impurity or defect in the crystal. Particularly, for the case of $(\text{Co}_{0.5}\text{Zn}_{0.5})_{20-x}\text{Mn}_x$ alloys, the end material $\text{Co}_{10}\text{Zn}_{10}$ has relatively small α [36] which might be advantageous to realize a larger nonreciprocity. In this respect, magnetic insulators typically have smaller α than metals where the magnon-electron scattering is inevitable. In fact, even for the case of Cu_2OSeO_3 , which shows rather small α comparable to yttrium gallium garnet [43], the strong-coupling condition $\alpha \ll \Delta\omega/\omega$ is not satisfied. This indicates that the magnon linewidth is an important factor even for discussing the phonon MChE in magnetic insulators.

Nevertheless, the phonon-MChE coefficient λ of $\text{Co}_9\text{Zn}_9\text{Mn}_2$ is 1.5 times larger than that of Cu_2OSeO_3 . This is because of the strong DM interaction in $\text{Co}_9\text{Zn}_9\text{Mn}_2$. By using the parameters summarized in Table I and Eq. (2), in fact, the expected g_{MChE} for $\text{Co}_9\text{Zn}_9\text{Mn}_2$ is four times larger than Cu_2OSeO_3 , assuming similar γ . Therefore, this system has a great potential to realize larger phonon MChE at room temperature, if the magnon linewidth could be controlled.

In conclusion, we demonstrate the phonon MChE, the nonreciprocal sound propagation in the chiral-lattice magnetic metal $\text{Co}_9\text{Zn}_9\text{Mn}_2$ up to 250 K. In contrast to the case in Cu_2OSeO_3 , the phonon MChE of $\text{Co}_9\text{Zn}_9\text{Mn}_2$ is enhanced at higher temperatures. This temperature dependence is due to the magnon linewidth. The magnon linewidth of $\text{Co}_9\text{Zn}_9\text{Mn}_2$ rapidly increases below 100 K and results in the weak coupling of the magnon-phonon hybridization, leading to the decreased gap and nonreciprocity. Controlling the magnon dispersion could fur-

ther enhance the nonreciprocal properties of these chiral crystals.

We thank N. Nagaosa for fruitful discussions. We acknowledge the support of the HLD at HZDR, member of the European Magnetic Field Laboratory (EMFL), and the DFG through the Collaborative Research Center

SFB 1143 (project-id 247310070). This work was partly supported by JSPS KAKENHI, Grant-in-Aid for Scientific Research (JP19K23421, JP20K14403, JP20H00349, JP20K15164, JP21H04440, JP21H04990, JP21K13876, JP21K18595), JSPS Bilateral Joint Research Projects (JPJSBP120193507), JST PRESTO (JPMJPR20B4), JST CREST (JPMJCR1874), and Katsu Research Encouragement Award of the University of Tokyo, Asahi Glass Foundation and Murata Science Foundation.

-
- [1] Y. Tokura and N. Nagaosa, *Nat. Commun.* **9**, 3740 (2018).
- [2] M. Atzori, C. Train, E. A. Hillard, N. Avarvari, and G. L. J. A. Rikken, *Chirality* **33**, 844–857 (2021).
- [3] G. L. J. A. Rikken and E. Raupach, *Nature (London)* **390**, 493–494 (1997).
- [4] M. Vallet, R. Ghosh, A. Le Floch, T. Ruchon, F. Bretenaker, and J. Y. Thépot, *Phys. Rev. Lett.* **87**, 183003 (2001).
- [5] C. Koerdt, G. Düchs, and G. L. J. A. Rikken, *Phys. Rev. Lett.* **91**, 073902 (2003).
- [6] C. Train, R. Gheorgh, V. Krstic, L. M. Chamoreau, N. S. Ovanesyan, G. L. J. A. Rikken, M. Gruselle, and M. Verdaguer, *Nat. Mater.* **7**, 729–734 (2008).
- [7] Y. Okamura, F. Kagawa, S. Seki, M. Kubota, M. Kawasaki, and Y. Tokura, *Phys. Rev. Lett.* **114**, 197202 (2015).
- [8] M. Atzori, H. D. Ludowieg, Á. Valentín-Pérez, M. Cortijo, I. Breslavetz, K. Paillot, P. Rosa, C. Train, J. Autschbach, E. A. Hillard, and G. L. J. A. Rikken, *Sci. Adv.* **7**, eabg2859 (2021).
- [9] G. L. J. A. Rikken, J. Fölling, and P. Wyder, *Phys. Rev. Lett.* **87**, 236602 (2001).
- [10] V. Krstic, S. Roth, M. Burghard, K. Kern, and G. L. J. A. Rikken, *J. Chem. Phys.* **117**, 11315–11319 (2002).
- [11] F. Pop, P. Auban-Senzier, E. Canadell, G. L. J. A. Rikken, and N. Avarvari, *Nat. Commun.* **5**, 3757 (2014).
- [12] T. Yokouchi, N. Kanazawa, A. Kikkawa, D. Morikawa, K. Shibata, T. Arima, Y. Taguchi, F. Kagawa, and Y. Tokura, *Nat. Commun.* **8**, 4757 (2017).
- [13] R. Aoki, Y. Kousaka, and Y. Togawa, *Phys. Rev. Lett.* **122**, 057206 (2019).
- [14] A. Kitaori, N. Kanazawa, H. Ishizuka, T. Yokouchi, N. Nagaosa, and Y. Tokura, *Phys. Rev. B* **103**, L220410 (2021).
- [15] S. Seki, Y. Okamura, K. Kondou, K. Shibata, M. Kubota, R. Takagi, F. Kagawa, M. Kawasaki, G. Tatara, Y. Otani, and Y. Tokura, *Phys. Rev. B* **93**, 235131 (2016).
- [16] R. Takagi, D. Morikawa, K. Karube, N. Kanazawa, K. Shibata, G. Tatara, Y. Tokunaga, T. Arima, Y. Taguchi, Y. Tokura, and S. Seki, *Phys. Rev. B* **95**, 220406(R) (2017).
- [17] Y. Iguchi, S. Uemura, K. Ueno, and Y. Onose, *Phys. Rev. B* **92**, 184419 (2015).
- [18] S. Seki, M. Garst, J. Waizner, R. Takagi, N. D. Khanh, Y. Okamura, K. Kondou, F. Kagawa, Y. Otani, and Y. Tokura, *Nat. Commun.* **11**, 256 (2020).
- [19] N. Ogawa, L. Köhler, M. Garst, S. Toyoda, S. Seki, and Y. Tokura, *Proc. Natl. Acad. Sci. U.S.A.* **118**, e2022927118 (2021).
- [20] T. Nomura, X.-X. Zhang, S. Zherlitsyn, J. Wosnitza, Y. Tokura, N. Nagaosa, and S. Seki, *Phys. Rev. Lett.* **122**, 145901 (2019).
- [21] A. A. Tereshchenko, A. S. Ovchinnikov, I. Proskurin, E. V. Sinitsyn, and J. Kishine, *Phys. Rev. B* **97**, 184303 (2018).
- [22] M. Kataoka, *J. Phys. Soc. Jpn.* **56**, 3635–3647 (1987).
- [23] J.-W. G. Bos, C. V. Colin, and T. T. M. Palstra, *Phys. Rev. B* **78**, 094416 (2008).
- [24] S. Seki, X. Z. Yu, S. Ishiwata, and Y. Tokura, *Science* **336**, 198–201 (2012).
- [25] T. Hori, H. Shiraisha, and Y. Ishii, *J. Magn. Magn. Mater.* **310**, 1820–1822 (2007).
- [26] W. Xie, S. Thimmaiah, J. Lamsal, J. Liu, T. W. Heitmann, D. Quirinale, A. I. Goldman, V. Pecharsky, and G. J. Millera, *Inorg. Chem.* **52**, 9399–9408 (2013).
- [27] Y. Tokunaga, X. Z. Yu, J. S. White, H. M. Rønnow, D. Morikawa, Y. Taguchi, and Y. Tokura, *Nat. Commun.* **6**, 7638–7644 (2015).
- [28] K. Karube, J. S. White, N. Reynolds, J. L. Gavilano, H. Oike, A. Kikkawa, F. Kagawa, Y. Tokunaga, H. M. Rønnow, Y. Tokura, and Y. Taguchi, *Nat. Mater.* **15**, 1237–1243 (2016).
- [29] K. Karube, J. S. White, D. Morikawa, M. Bartkowiak, A. Kikkawa, Y. Tokunaga, T. Arima, H. M. Rønnow, Y. Tokura, and Y. Taguchi, *Phys. Rev. Mater.* **1**, 074405 (2017).
- [30] D. Morikawa, X. Yu, K. Karube, Y. Tokunaga, Y. Taguchi, T. Arima, and Y. Tokura, *Nano Lett.* **17**, 1637–1641 (2017).
- [31] X. Z. Yu, W. Koshibae, Y. Tokunaga, K. Shibata, Y. Taguchi, N. Nagaosa, and Y. Tokura, *Nature (London)* **564**, 95 (2018).
- [32] K. Karube, J. S. White, D. Morikawa, C. D. Dewhurst, R. Cubitt, A. Kikkawa, X. Yu, Y. Tokunaga, T. Arima, H. M. Rønnow, Y. Tokura, and Y. Taguchi, *Sci. Adv.* **4**: eaar7043 (2018).
- [33] T. Nagase, M. Komatsu, Y. G. So, T. Ishida, H. Yoshida, Y. Kawaguchi, Y. Tanaka, K. Saitoh, N. Ikarashi, M. Kuwahara, and M. Nagao, *Phys. Rev. Lett.* **123**, 137203 (2019).
- [34] K. Karube, J. S. White, V. Ukleev, C. D. Dewhurst, R. Cubitt, A. Kikkawa, Y. Tokunaga, H. M. Rønnow, Y. Tokura, and Y. Taguchi, *Phys. Rev. B* **102**, 064408 (2020).
- [35] T. Nagase, Y. G. So, H. Yasui, T. Ishida, H. K. Yoshida, Y. Tanaka, K. Saitoh, N. Ikarashi, Y. Kawaguchi, M. Kuwahara, and M. Nagao, *Nat. Commun.* **12**, 3490

- (2021).
- [36] M. Preißinger, K. Karube, D. Ehlers, B. Szigeti, H.-A. Krug von Nidda, J. S. White, V. Ukleev, H. M. Rønnow, Y. Tokunaga, A. Kikkawa, Y. Tokura, Y. Taguchi, and I. Kézsmárki, *npj Quantum Materials* **6**:65 (2021).
 - [37] L. C. Peng, K. Karube, Y. Taguchi, N. Nagaosa, Y. Tokura, and X. Z. Yu, *Nat. Commun.* **12**, 6797 (2021).
 - [38] T. Shimojima, A. Nakamura, X. Z. Yu, K. Karube, Y. Taguchi, Y. Tokura, and K. Ishizaka, *Sci. Adv.* **7**, eabg1322 (2021).
 - [39] S. Zherlitsyn, S. Yasin, J. Wosnitza, A. A. Zvyagin, A. V. Andreev, and V. Tsurkan, *Low Temp. Phys.* **40**, 123-133 (2014).
 - [40] R. Takagi, M. Garst, J. Sahliger, C. H. Back, Y. Tokura, and S. Seki, *Phys. Rev. B* **104**, 144410 (2021).
 - [41] See Supplemental Material at <http://> for the experimental details and theoretical derivation of the anticrossing gap at the magnon-phonon hybridization.
 - [42] Y. Hirokane, Y. Nii, H. Masuda, and Y. Onose, *Sci. Adv.* **6**, eabd3703 (2020).
 - [43] I. Stasinopoulos, S. Weichselbaumer, A. Bauer, J. Waizner, H. Berger, S. Maendl, M. Garst, C. Pfleiderer, and D. Grundler, *Appl. Phys. Lett.* **111**, 032408 (2017).
 - [44] H. Yu, R. Huber, T. Schwarze, F. Brandl, T. Rapp, P. Berberich, G. Duerr, and D. Grundler, *Appl. Phys. Lett.* **100**, 262412 (2012).
 - [45] K. Gilmore, M. D. Stiles, J. Seib, D. Steiauf, and M. Fähnle, *Phys. Rev. B* **81**, 174414 (2010).
 - [46] T. Kikkawa, K. Shen, B. Flebus, R. A. Duine, K. Uchida, Z. Qiu, G. E. W. Bauer, and E. Saitoh, *Phys. Rev. Lett.* **117**, 207203 (2016).
 - [47] B. Flebus, K. Shen, T. Kikkawa, K. Uchida, Z. Qiu, E. Saitoh, R. A. Duine, and G. E. W. Bauer, *Phys. Rev. B* **95**, 144420 (2017).
 - [48] C. Kittel, *Phys. Rev.* **110**, 836–841 (1958).

Supplemental Material of "Nonreciprocal Phonon Propagation in a Metallic Chiral Magnet"

(Dated: December 2, 2022)

This Supplemental Material will be separated in the published manuscript.

Acoustic-mode dependence of the ultrasound results

Figure S1(a) shows the sound-velocity change of $\text{Co}_9\text{Zn}_9\text{Mn}_2$ as a function of magnetic fields $\Delta v/v_0(H)$ at 4 K. Here, we present the results for the three acoustic modes; $c_L = (c_{11} + c_{12} + 2c_{44})/2$ ($\mathbf{k}||\mathbf{u}||[110]$, $v = 4.0$ km/s), $c_T = (c_{11} - c_{12})/2$ ($\mathbf{k}||[110]$, $\mathbf{u}||[1\bar{1}0]$, $v = 2.1$ km/s), and c_{44} ($\mathbf{k}||[110]$, $\mathbf{u}||[001]$, $v = 2.4$ km/s), where \mathbf{k} and \mathbf{u} are the propagation and displacement vectors, respectively. A magnetic transition at 0.21 T, where the magnetic state changes from a helical to collinear states, is observed for these acoustic modes. The magnitude of the anomaly $\Delta v/v_0(H_c)$ is rather small for the longitudinal mode c_L , indicating that the magnetoelastic coupling is weak for the longitudinal strains. The temperature dependence of $\Delta v/v_0(H_c)$ is plotted in Fig. S1(b). The c_{44} mode shows the largest acoustic response in the whole temperature range. The phonon magnetochiral effect (MChE) is discussed only for the transverse modes, c_{44} and c_T .

Phonon magnetochiral effect

Here, we present the temperature dependences of the phonon MChE for the c_{44} and c_T modes. Figures S2 and S3 summarize the results on the c_{44} and c_T modes, respectively. Both acoustic modes show similar temperature dependence of $\Delta v/v_0(H)$. The anomaly at the transition field becomes larger at intermediate temperatures (90 K for the c_{44} and 30 K for the c_T modes) and rapidly becomes weak at higher temperatures (260 K for the c_{44} and 200 K for the c_T modes) [Figs. S2(a) and S3(a)]. Phonon MChE is observed for both acoustic modes with the same sign [Figs. S2(b) and S3(b)]. Frequency and temperature dependences of the magnitude of the phonon MChE are summarized in Figs. S2(c, d) and S3(c, d). The frequency dependence is reasonably fitted by Eq. (2) in the main text, indicating that the mechanism of this nonreciprocity is the magnon-phonon hybridization [20].

Temperature dependence of the acoustic attenuation

In this study, we discuss the results of the MChE only up to 250 K. This is because the acoustic attenuation becomes significantly large at above 260 K, and

the high-frequency measurement is not possible. Besides, the magnitude of the anomaly at the transition $\Delta v/v_0(H_c)$ becomes rapidly small around this temperature [Fig. S1(b)]. Here, we present the temperature dependence of the ultrasound echo amplitude and discuss why the attenuation increases around this temperature.

Figure S4 shows the temperature dependence of the relative change of the sound velocity $\Delta v/v_0(T)$ and echo-signal amplitude of the c_{44} mode at zero field. The measurements were performed at 180 and 94 MHz to prove the reproducibility. Both results show significant signal decrease around 260 K. In the same temperature range, sound velocity also shows kink-like structures. We should note that these behaviors might come from extrinsic origins (ex. glass transition of the glue connecting the sample and transducers, which occurs around 300 K). Note, any other magnetic probes (magnetization and ferromagnetic resonance) do not show anomalous behavior at this temperature [29, 36]. Another possibility is that the temperature dependence of the magnetic anisotropy [36]. The magnetic anisotropy of $\text{Co}_9\text{Zn}_9\text{Mn}_2$ decreases towards higher temperatures, and the potential barrier to flip magnetization becomes already rather small around 260 K. Since the magnitude of the anomaly $\Delta v/v_0(H_c)$ is related to the change of magnetization $\Delta M(H_c)$, the acoustic response might also become small in this temperature range.

Estimation of the repulsion scale caused by the magnon-phonon hybridization

Here we follow the magnon-phonon coupling theory [20] to discuss the scale of the repulsion gap. To make an order of magnitude estimation, it suffices to compare the hybridized dispersion and the unhybridized phonon dispersion at the point where the unhybridized phonon and magnon dispersions cross each other. To this end, we cannot use the perturbative low-energy dispersion expressions since the anticrossing is far away from the origin $k = 0$.

We will use the shorthand $k = (k_z, \mathbf{z})$ for Fourier transform, in which \mathbf{z} is the generic complex frequency or the Matsubara frequency $i\omega$. For the real fields u^i , we simply stick to $u^i = \sum_k e^{-i\omega\tau + ik_z z} u_k^i$ and have $u_k^{i*} = u_{-k}^i$. We also use $a = \sum_k e^{-i\omega\tau + ik_z z} a_k$, $\bar{a} = \sum_k e^{i\omega\tau - ik_z z} \bar{a}_k$ and obviously $a_k^* = \bar{a}_k$. Let us proceed to write down the full Lagrangian in the imaginary time. The TA phonon reads $\mathcal{L}_{\text{ph}} = \frac{1}{2} [\rho(\partial_\tau \bar{u})^2 + c|\nabla \bar{u}|^2]$ with $|\nabla \bar{u}|^2 = \partial^j u_i \partial_j u^i$ and the phonon velocity $v_0 = \sqrt{c/\rho}$. It is convenient to use the Holstein-Primakov representation $S^x = \sqrt{S/2}(\bar{a} + a)$, $S^y = i\sqrt{S/2}(\bar{a} - a)$ and

$S^z = S - \bar{a}a$ in the induced collinear state. Then the pure spin-wave theory reads $\mathcal{L}_{\text{sw}} = \frac{1}{V_0}(\hbar\bar{a}\partial_\tau a + 2SJa_0^2\nabla\bar{a}\nabla a + 2iSDa_0\bar{a}\partial_z a + gB\bar{a}a)$. The magnon dispersion is $\omega_{\text{mag}}(k_z) = b - \sigma\text{sgn}(\vec{k}\cdot\vec{B})v_{\text{DM}}|k_z| + w_{\text{EX}}k_z^2$, in which $b = \Delta_B/\hbar$ with the Zeeman energy gap $\Delta_B = gB$ and we define $v_{\text{DM}} = 2SDa_0/\hbar$, $w_{\text{EX}} = 2SJa_0^2/\hbar$ for later convenience.

The corresponding actions in energy-momentum space are $\mathcal{S}_{\text{ph}} = \frac{1}{2}\sum_k \bar{u}_k^\dagger M_k^{\text{ph}} \vec{u}_k$, $\mathcal{S}_{\text{sw}} = \sum_k \bar{a}_k M_k^{\text{sw}} a_k$, $\mathcal{S}_{\text{me}} = \frac{1}{\sqrt{2}}\sum_k i\alpha k_z^2(\nu_{-k}a_k - \bar{a}_k\bar{\nu}_k)$ with $\alpha = \langle S^z \rangle \sqrt{SD}/a_0^2$. Here, we define the circularly polarized basis $\nu = u^x - iu^y$, $\bar{\nu} = u^x + iu^y$, $\vec{\nu}_k = (\nu_{-k}, \bar{\nu}_k)^T$ and obviously $\nu_k^* = \bar{\nu}_{-k}$. We can further obtain the hybridized phonon action $\mathcal{S} = \mathcal{S}_{\text{ph}} - \frac{1}{2}\sum_k \alpha^2 k_z^4 \nu_{-k} (M_k^{\text{sw}})^{-1} \bar{\nu}_k$ with a new action matrix $M_k = M_k^{\text{ph}} - \frac{\alpha^2 k_z^4}{M_k^{\text{sw}}} \begin{bmatrix} 1 & i \\ -i & 1 \end{bmatrix}$. Because of the chiral magnetoelastic coupling, only the left and right circularly polarized TA phonons (LCP and RCP) are the eigenstates instead of the completely degenerate case of the pure phonon theory. This implies the reformulation $\mathcal{S} = \frac{1}{2}\sum_k \bar{\nu}_k^\dagger \tilde{M}_k \vec{\nu}_k$ via a unitary transformation to the circularly polarized basis.

From the dispersion equation $\det \tilde{M}_k = 0$ of the hybridized modes, we can obtain the following with the generic complex frequency z replaced by real ω and the momentum along \hat{z} -axis by k

$$\omega^2 - \omega_0^2(k) - \frac{2\tilde{\alpha}^2 k^4}{\omega - \omega_{\text{mag}}(k)} = 0 \quad (5)$$

where $\omega_0 = v_0 k$, ω_{mag} are respectively the original phonon and magnon dispersions that cross at momentum k^* and $\tilde{\alpha}^2 = \alpha^2/(\rho s)$ is the rescaled coupling constant with $s = \hbar/V_0$. For simplicity, we henceforth consider only the anticrossing gap at $k > 0$ with $\mathbf{k} \parallel \mathbf{B}$ and crystal chirality $\sigma = 1$. At k^* , the equation becomes

$$(\omega + \omega^*)(\omega - \omega^*)^2 - 2\tilde{\alpha}^2 k^{*4} = 0 \quad (6)$$

with $\omega^* = \omega_0(k^*)$. Then we obtain a good approximation

$$|\omega - \omega^*| = \sqrt{\frac{2\tilde{\alpha}^2 k^{*4}}{\omega + \omega^*}} \approx \frac{\tilde{\alpha} k^{*2}}{\sqrt{\omega^*}}, \quad (7)$$

which can be rewritten as

$$|\omega - \omega^*| = \frac{\gamma \langle S^z \rangle \sqrt{SD}}{a_0^2 \sqrt{\rho s v_0}} k^{*\frac{3}{2}} = \frac{\gamma \langle S^z \rangle \sqrt{SD}}{a_0^2 \sqrt{\rho s v_0^2}} \omega^{*\frac{3}{2}} \quad (8)$$

and is manifestly proportional to the coupling strength γ . The only task left is to calculate k^* . Typically, the exchange interaction term in ω_{mag} , i.e., w_{EX} , can be neglected, we therefore have $k^* = \frac{b}{v+v_{\text{DM}}}$.

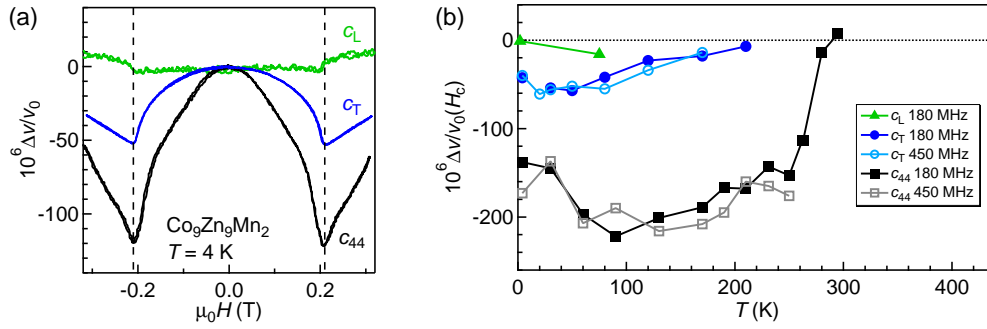


Fig. S 1. (a) Acoustic-mode dependence of the sound velocity change $\Delta v/v_0(H)$ at 4 K. (b) Temperature dependence of the sound velocity change at the transition field $\Delta v/v_0(H_c)$. The acoustic mode and ultrasound frequency are denoted in the caption.

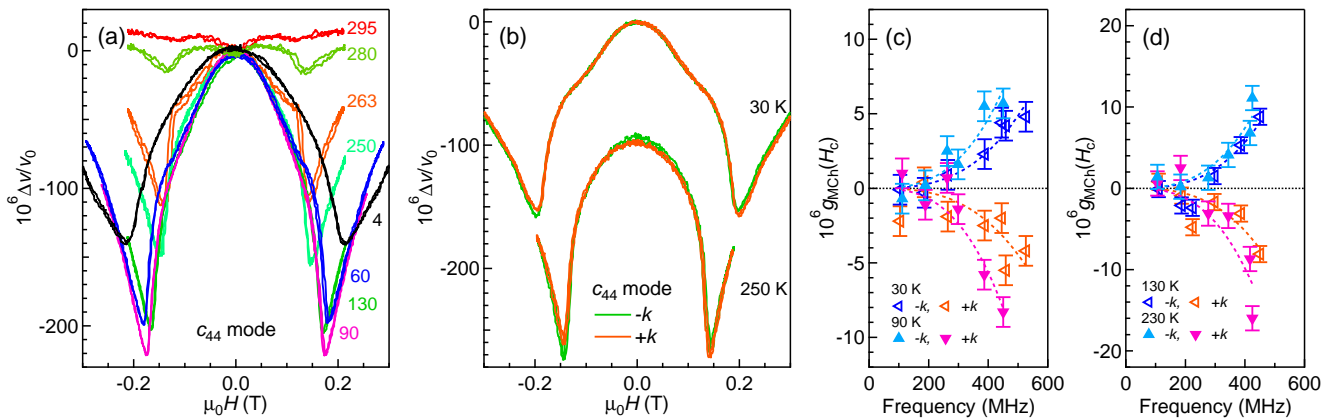


Fig. S 2. Summary of the ultrasound results on the c_{44} mode. (a) $\Delta v/v_0(H)$ curves measured at selected temperatures for the c_{44} mode at 180 MHz. (b) Phonon MChE observed at 30 K (526 MHz) and 250 K (434 MHz). The results for $-k$ (green) and $+k$ (orange) are shown. (c, d) Frequency and temperature dependence of the magnitude of the MChE at the transition field $g_{MCh}(H_c)$. The dashed lines show the fitting curve based on Eq. (2).

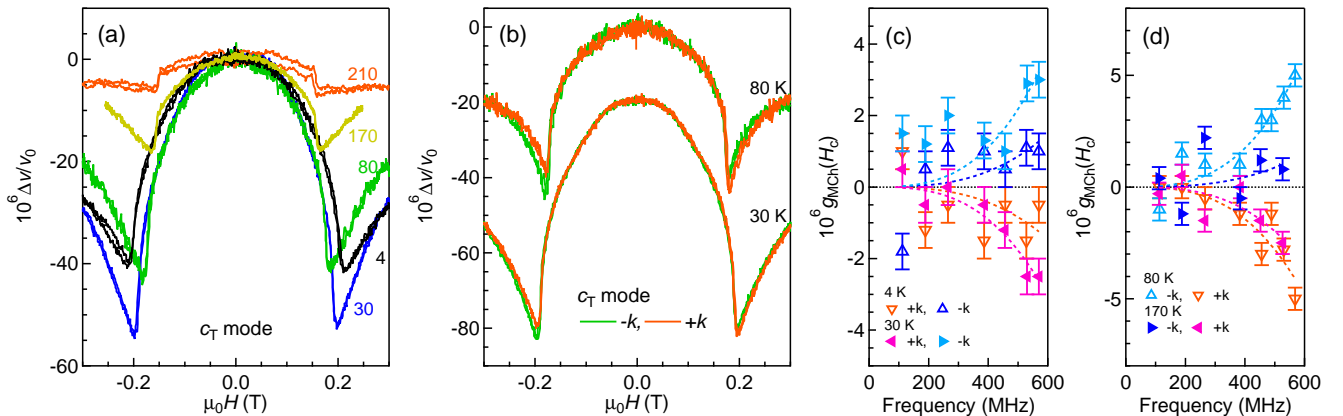


Fig. S 3. Summary of the ultrasound results on the c_T mode. (a) $\Delta v/v_0(H)$ curves measured at selected temperatures for the c_T mode at 180 MHz. (b) Phonon MChE observed at 30 K (530 MHz) and 80 K (568 MHz). The results for $-k$ (green) and $+k$ (orange) are shown. (c, d) Frequency and temperature dependence of the magnitude of the MChE at the transition field $g_{MCh}(H_c)$. The dashed lines show the fitting curve based on Eq. (2).

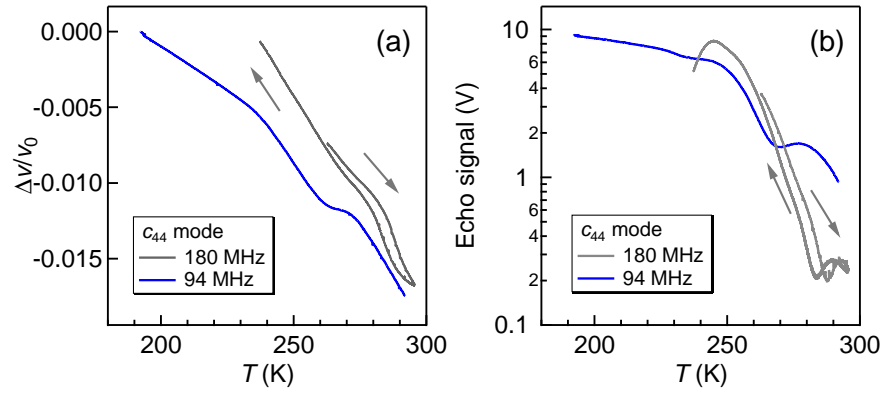


Fig. S 4. Temperature dependence of the (a) sound velocity and (b) echo signal amplitude of the c_{44} mode measured at 180 and 94 MHz.